Case Studies in Thermal Engineering 28 (2021) 101445

Contents lists available at ScienceDirect

Case Studies in Thermal Engineering

journal homepage: www.elsevier.com/locate/csite

Heat exchange enhancement of jet impingement cooling with the novel humped-cone heat sink

Marcin Froissart [a,*], Paweł Ziółkowski [b], Waldemar Dudda [c], Janusz Badur [a]

[a] Institute of Fluid-Flow Machinery, Polish Academy of Sciences, 14 Fiszera Street, Gdańsk 80-231, Poland
[b] Faculty of Mechanical Engineering and Ship Technology, Gdańsk University of Technology, 11/12 Gabriela Narutowicza Street, 80-233 Gdańsk, Poland
[c] Faculty of Technical Sciences, University of Warmia and Mazury in Olsztyn, 11E Oczapowskiego Street, 10-736 Olsztyn, Poland

ARTICLE INFO

Keywords:
Cone heat sink
Jet impingement
Heat transfer improvement
Numerical simulation
Boundary layer reduction

ABSTRACT

Jet impingement cooling technology is applicable to control temperature of devices, where very high heat flux is generated within a small area. This paper is about the improvement of the jet impingement cooling efficiency by the heat sink geometry modification. Two reference cases were sourced from the literature – flat heat sink and modified one with cone in the jet stagnation region. Such a change improves cooling capability by more than 10%. Presented thermal fluid-solid interaction numerical results are focused to understand better the physics of that improvement and proposed the next step of shape optimization.

Two geometrical parameters were investigated – cooling channel's height and cone's side wall deformation radius. That includes twenty radiuses for each of three heights. Together with two reference cases, sixty-two shapes were analysed. Such extensive parametrical study was possible thanks to the usage of 2D axisymmetric model, which very well matched to the referenced 3D analysis and experiment. It was concluded, that cone deformation impact varies with the cooling channel's height. For the optimum geometrical configuration, 11% cooling capability improvement was concluded in comparison to the reference flat surface (8% due to the channel height's reduction and 3% due to the cone's deformation).

1. Introduction

Jet impingement concept is known for decades and is used successfully in many industries. It includes thermal drying of continuous sheets, turbine cooling, de-icing of aircraft wings and cooling of microprocessors. Variety of fluids are used as a working medium. As an example, Badur and Bryk [1] concluded that certain steam injection can help to reduce steam turbine acceleration time by one third. Water is one of the most accessible and efficient heat transfer fluids. Its specific heat capacity is few times larger than gas alternatives, so it is often used in heat transfer experiments. Tang et al. [2] used it in the jet impingement experiment using a novel single cone heat sink. In general, such cooling system is applicable to the devices where very dense heat flux is generated, so the excessive heat cannot be transferred by the heat exchange surface extension. The examples of jet impingement cooling application are highly integrated electronic devices, microelectromechanical systems, high-power lasers and highly thermally loaded turbine components like blades

* Corresponding author.
E-mail addresses: marcin.froissart@imp.gda.pl (M. Froissart), pawel.ziolkowski1@pg.edu.pl (P. Ziółkowski), dudda@uwm.edu.pl (W. Dudda), janusz.badur@imp.gda.pl (J. Badur).

https://doi.org/10.1016/j.csite.2021.101445
Received 18 June 2021; Received in revised form 28 August 2021; Accepted 11 September 2021
Available online 13 September 2021

Nomenclature

H	height, mm
R	radius, mm
v	velocity, m/s
Nu	Nusselt number,
$\overline{Nu}$	area-averaged Nusselt Number,
Nu_r	Nusselt number at given radius,
h	heat transfer coefficient, W/(m^{2}K)
$\overline{h}$	area-averaged heat transfer coefficient, W/(m^{2}K)
h_r	heat transfer coefficient at given radius, W/(m^{2}K)
q	heat flux, W/m^2
$\overline{q}_{sn}$	normal area-averaged surface heat flux, W/m^2
q_{rn}	normal heat flux at given radius, W/m^2
T	temperature, K
$\overline{T_s}$	area-averaged surface temperature, K
T_r	temperature at given radius, K
T_j	jet temperature, K
L	characteristic length, m
r	radius, mm
p	pressure, Pa
I	unit tensor,
t^{t}	total viscous stress tensor, Pa
b	gravitation force, N
e	the sum of specific internal and specific kinetic energy, J/kg
q^t	total heat flux, W/m^2
$\mathbf{J}_k$	diffusion flux of turbulent kinetic energy k, 1/s^3
$\mathbf{J}_\varepsilon$	diffusion flux of kinetic energy dissipation ε, 1/s^4
S_k	source of turbulent kinetic energy, m^2/s^3
S_ε	source of turbulent kinetic energy dissipation, m^2/s^4
$Nu_{rAN\,i}$	area-normalized local Nusselt number,
$Nu_{r\,i}$	local Nusselt number at given radius,
$r_{\,i}$	local heat sink radius, m
$r_{\,i-1}$	local heat sink radius preceding to $r_{\,i}$, m

Greek symbols

α	angle, deg
λ	thermal conductivity, W/mK
ρ	density, kg/m^3

Acronyms

FSI	fluid-solid interaction
CFD	computational fluid dynamics
PTC	positive temperature coefficient
2D	two-dimensional
3D	three-dimensional
FEA	finite element analysis
CSD	computational solid dynamics
FVM	finite volume method
RNG	renormalization group
RANS	Reynolds-averaged Navier-Stokes
Y^+	wall function
SIMPLE	semi-implicit method for pressure-linked equations

Subscripts and superscripts

i	index
r	radius
s	surface
j	jet
k	kinetic energy

ε	kinetic energy dissipation
AN	area-normalized
t	total
n	normal

and inner casings. The motivation of presented work is further improvement of jet impingement cooling system by changing shape of the heat sink. Thanks to that, gas engines could be operated at higher efficiency (higher temperature) and microprocessors could work at a higher load.

Thermal Fluid-Solid Interaction (FSI) is an analysis method which offers a proper micro/nanoscale description of heat transfer phenomena across the boundary between solid and fluid. Badur et al. [3] discussed and implemented an advanced Reynolds-Stanton analogy to improve mathematical modelling of thermal energy transportation.

Basic jet impingement cooling concept contains a jet of fluid which impinges into flat surface at 90 deg. angle. However various modifications of it are the subject of extensive worldwide research programmes. Sharif and Afroz [4] reported average Nusselt number for twin opposite directed impingement jets concluded that 90 deg. angle is the most efficient one. Attalla et al. [5] reported average Nusselt number for twin parallel jets and found that the most efficient angle varies between 0 and 20 deg., as it depends on jets' size and position. Draksler et al. [6] investigated multiple impinging jets in hexagonal configuration. Nusselt Number distribution plot revealed that large-eddy structures augment local heat transfer also in areas between jets. He and Liu [7] investigated jet impingement cooling using lobed nozzles. They concluded that shape has some impact at low nozzle-to-wall distance, but average Nusselt number improvement is within few percent. Baghel et al. [8] analysed inclined free surface liquid jet impingement. They found that peak Nusselt number decreases from 0 deg. to 15 deg. then it increases until the inclination angle of 45 deg. Xu et al. [9] reported that finned target surface can improve Nusselt number significantly for the optimized fin width and height. Yang and Peng [10] performed a study of non-uniform fin height heat sink. Obtained results show that most of analysed cases are worse than the uniform pin-fin heat sink. Only few configurations are slightly more efficient than reference uniform case. Choo et al. [11] experimentally tested air assisted free water jet impingement at low nozzle-to-surface distances. It was found that stagnation Nusselt number increases significantly for very low distances (below 0.1 of inlet diameter).

Hu et al. [12] modelled surface roughness with sinusoidal wave. They concluded that roughness plays dominant role in the cooling effectiveness. Sundararajan et al. [13] experimentally tested jet impingement into rough surface. It was found that multi-protrusions case increases more heat transfer coefficient than can be attributed to the area enlargement. Singh et al. [14] checked the correlation between the micro-roughness shapes and jet impingement heat transfer enhancement. It was found that concentric shapes are more efficient than traditional cubic and cylindrical ones. Ortega-Casanova and Molina-Gonzales [15] found that concentric tabs around the stagnation point always reduce average cooling effectiveness in comparison to the flat surface. Rao et al. [16] analysed a row of impingement jets cooling flat and roughened surface. They found that micro W-shaped ribs can enhance heat transfer coefficient by nearly 10% with negligibly increased pressure loss. Li et al. [17] investigated the impingement heat transfer in a high-pressure turbine inner casting. They concluded that cambered rib structure increases average Nusselt number significantly in comparison to the smooth surface.

Singh and Ekkad [18] tested and analysed the cross-flow impact to the multiple impingement jet cooling configuration. They found an interesting trend that a maximum crossflow was more efficient than intermediate crossflow scheme. Ligrani et al. [19] found that in general crossflow is detrimental to the local Nusselt number performance, but for some tested configurations crossflow fluid results in the opposite trend. Sunden et al. [20–22] tested and analysed the vortex generator pair, which reduces the detrimental crossflow impact. They found that delta and rectangular winglets can significantly augment the jet impingement heat transfer by promoting the jet penetration.

Li et al. [23] performed a comparative study on gas turbine leading edge cooling. They concluded that single vortex cooling has the highest heat transfer coefficient but the highest-pressure loss. It appeared that middle-double vertex cooling is the best compromise between cooling efficiency and pressure drop. Azimi et al. [24] investigated slot jet impingement of a concave surface. The maximum Nusselt number has been obtained at the stagnation point and monotonically decreased along the concave surface. Liu et al. [25] analysed jet impingement cooling on the concave surface. They found that spanwise jets' offset can enhance cooling effectiveness for low Reynolds numbers. Zeng et al. [26] performed a numerical investigation of mist/air impingement cooling on ribbed concave surface. They found that air/mist two-phase flow is more efficient than single-phase case with the penalty of increased pressure drop. Zhang et al. [27] analysed case of impingement jet heating of engine inlet guide strut. They found that heating effectiveness is tightly dependent on the normal jet-to-impinged surface distance. Sunden et al. [28] studied the jet impingement cooling characteristics in a rotating chamber. Due to the Coriolis and centrifugal forces, stagnation points were shifted downstream, which resulted in crooked cooling jets and impingement reduction.

Wang et al. [29] investigated turbine leading edge interaction between jet impingement and effusion cooling. They found that film cooling holes act like coolants' interceptors, so mass flow is highly dependent on the distance from the stagnation region. Cho et al. [30] optimized the impingement/effusion cooling system to minimise thermal stress. They observed that very high stresses occur near the film cooling hole, even for the low average temperature. Zu et al. [31] investigated integrated impingement/pin/effusion cooling configurations. They proved that installing an array of cylindrical pins to the double-wall impingement/effusion structure is beneficial.

Nasif et al. [32] simulated jet impingement heat transfer onto a moving disc. It was found that the relative velocity increase enhances the cooling efficiency. Jeng et al. [33] investigated jet impingement into a rotating pin-fin heat sink. They concluded that average Nusselt number can grow or drop with the increase of rotational Reynolds number, which is a function of tested geometry.

Muszynski and Mikielewicz [34] studied the microjet array cooling system. They proposed a Nusselt number analytical correlation which agreed with the experiment within 30% error bounds.

Wongcharee et al. [35]. investigated the effect of using swirling impingement jet generated by the threaded nozzle. For the investigated cases, the jet delivered through the twisted lobed nozzle with twist ratio of four yielded a maximum average Nusselt number. Xu et al. [36] performed a similar investigation, concluding that the local Nusselt number at the stagnation point of the swirling impingement jet with the swirl angle of 45 deg. is 11.4% higher than for the conventional circular jet. Amini et al. [37] extended swirling jet analysis by a pair-of-jets interaction study. By doing this they obtained a heat transfer enhancement up to 10%.

The main objective of this paper is to explore the heat sink shape's impact into the water jet impingement cooling enhancement. Presented study is based on 2D axisymmetric thermal-FSI model, which was validated against the Tang et al. [2] experiment. They concluded that an area-averaged Nusselt number is improved by 8% by adding 45° cone in the stagnation area. Equally important, this study resulted with creation and validation of thermal-FSI model, which can be used in further assessments of heat sink shape modifications. The additional goal is to support the advanced thermal-FSI extension proposed in works [3,38], which so far has been used for steam and gas turbine analyses [39,40]. Ziółkowski et al. [41] explored the gas turbine heat recovery system proposed by Szewalski. Some forms of analysed impingement cooling can be used in heat exchangers aimed to increase Bryton cycle's efficiency.

Due to the analysed size of the humped-cone heat sink, local recirculation zones can be considered as a microflow. In recent years, numerous state-of-the-art papers were published in the field of microflows and nanofluids, which contain tiny nanoparticles. Zhang et al. [42] analysed the magnetic effects of zinc/aluminium-oxide kerosene nanofluid flowing over complex surfaces with stretching and shrinking features. They found that the velocity and temperature profiles are enhanced or reduced (depends on the geometry) by increasing the magnetic field parameter. Same author examined also the electro-magnetohydrodynamic non-Newtonian fluid flow [43] through the porous material fixed between a pair of two parallel plates. They concluded that the presence of the magnetic field enhances the temperature profile but retards the velocity profile due to the opposite Lorentz force. Abo-Elkhair et al. [44] studied the magnetic force effects of hybrid bio-nanofluid (Au–Cu). Using the Adomian decomposition method they obtained expressions of velocity, induced magnetic field components, magnetic pressure, stream function, magnetic force, joule heating, shear stress and Nusselt number. Bhatti et al. [45] studied the Arrhenlus activation energy on the thermo-bioconvection nanofluid flow over a Riga plate. They found that the velocity profile strengthens with the increase of the bioconvection Rayleigh number and magnetic field. Badur et al. [46]. considered the Navier-Stokes slip boundary conditions following from the mass and momentum balances within a thin, shell-like moving boundary layer. They classified different mobility mechanisms connected with the transpiration phenomena, important for flows in micro- and nanochannels. Same author [47] reformulated basic concepts of fluid mechanics in order to account some enhancement phenomena in micro- and nanoflows. Work [48] is based on the thermal transpiration approach developed in Ref. [46]. The microscale transient calculation was compared against the experiment and theory proposed by Reynolds. On top of that, Badur et al. [49] extended a general form of surface forces (friction and mobility component) to collect the effects of bulk and surface fluid motion.

This paper's structure is as follows. Section 1 presents the literature overview describing various aspects of fluid's jet impingement. The experiment details are shortly presented in Section 2. Section 3 contains a brief summary of the thermal-FSI approach taken in this study. The results exposition is given in Section 4. Concluding remarks are formulated in Section 5.

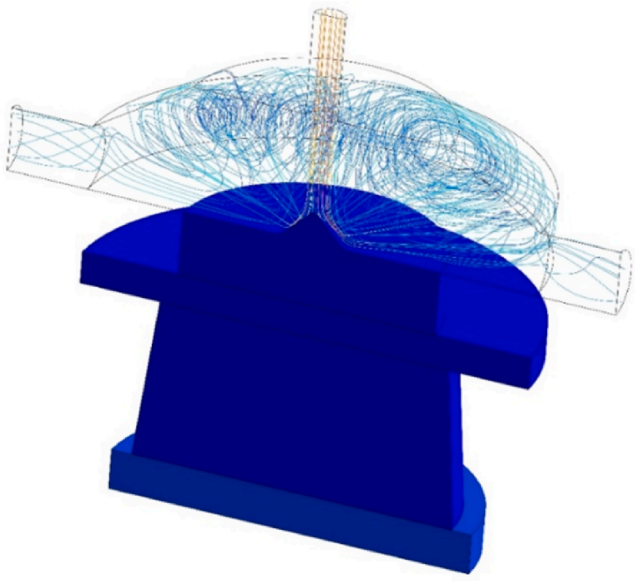

Fig. 1. Structure of the single cone heat sink jet device (symmetrical view).

2. Model validation

Results presented in this paper are based on an experiment performed by Tang et al. [2], where the surface of the heat sink is cooled by the water jet impingement. The comparison between flat ($\alpha = 0$ deg.) and conical ($\alpha = 45$ deg.) surface revealed that cooling efficiency was improved by 8.5%.

It was decided to conduct an analytical study to improve the shape of the novel single cone heat sink concept. To make this happen, a 2D axisymmetric preliminary thermal-FSI model was built and validated against Tang et al. [2] experiment. That is a crucial part of presented study, as every viscous model available in CFD software is an approximation of a complex physical processes.

2.1. Jet device

Single cone heat sink jet device presented on Fig. 1 was tested by Tang et al. [2]. It contains solid blocks at the bottom and a cooling channel at the top. Aluminium base is heated by the PTC (positive temperature coefficient) heater with the constant heat flux density $q = 80$ W/cm^2, which is conducted through adjacent blocks towards the heat sink at the top. Impingement surface is an area where heat is absorbed by the water stream and transported towards the outlet pipes. Fig. 1 presents symmetrical view of stream flow, which is injected at the top ($\mathbf{v} = 6$ m/s), dispersed radially at the cone, recirculated at the side surface and redirected towards outlet pipes.

Fig. 2 and Table 1 show key dimensions of analysed heat sink. Angle $\alpha = 0$ deg. is a reference flat surface. For all other analysed cases $\alpha = 45$ deg. was used. The difference between tested and modelled cases is the R_3 arc which is situated exactly at the lower half of the cone's surface.

Fig. 2 presents the section of the actual heat sink, which is not an axisymmetric geometry (compare with Fig. 1 3D view). Two outlet pipes are the only non-axisymmetric feature, so it was decided to convert them for analysis to the one continuous ring with the consistent exit area.

2.2. Criteria number

An area-averaged Nusselt number was used as a criterium for the cooling enhancement assessment. According to Tang et al. experiment [2], average Nusselt number for the flat surface is 1238.7 in contrast to the 1373.7 for the 45deg. conical case.

The local Nusselt number at given radius can be calculated according to (1):

$$Nu_r = \frac{h_r L}{\lambda} = \frac{q_{rn} L}{\lambda \left(T_r - T_j\right)} \tag{1}$$

where Nu_r is a Nusselt number at given radius [−], h_r is a heat transfer coefficient at given radius [W/(m^{2}K)], q_{rn} represents normal heat flux at given radius [W/m^2], T_r is a temperature at given radius [K], T_j represents jet temperature [K]. For analysed case, characteristic length (heat sink diameter) L = 0.032 m and water thermal conductivity $\lambda = 0.6$ W/mK.

Area-averaged Nusselt number can be calculated according to (2):

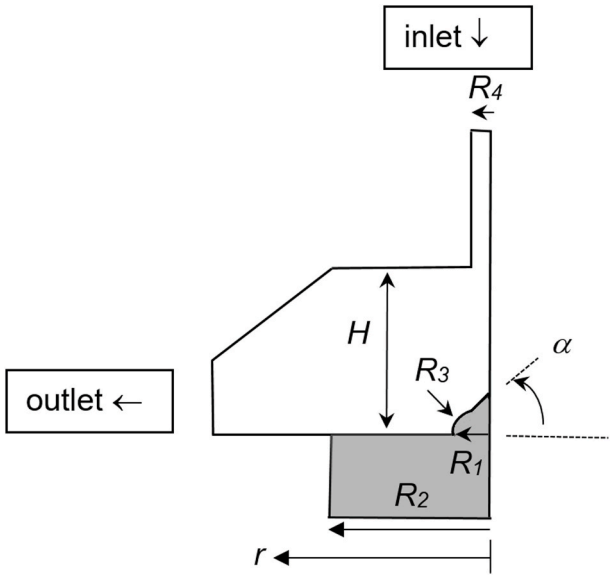

Fig. 2. Heat sink key dimensions.

Table 1
Heat sink experimental parameters.

α [deg]	R_4 [mm]	R_1 [mm]	R_2 [mm]	R_3 [mm]	H [mm]	**v** [m/s]	q [W/cm^2]
45 and 0	2	4	16	none (flat)	16	6	80

$$\overline{Nu} = \frac{\overline{h}\,L}{\lambda} = \frac{\overline{q}_{sn} L}{\lambda\left(\overline{T_s} - T_j\right)} \tag{2}$$

where $\overline{Nu}$ is an area-averaged Nusselt Number [−], $\overline{h}$ represents area-averaged heat transfer coefficient [W/(m^{2}K)], $\overline{q}_{sn}$ is a normal area-averaged surface heat flux [W/(m^2)], $\overline{T_s}$ represents area-averaged surface temperature [K].

3. Analysis

Analysed preliminary thermal-FSI model is based on heat sink device tested by Tang et al. [2]. It was concluded that geometry presented on Fig. 1 is very close to the axisymmetric case, so 2D finite element analysis (FEA) model was build. This was done in contrast to Tang et al. approach [2], where 3D section was modelled. Comparison revealed that 2D axisymmetric result is very close to the experiment and 3D model, so it was used for further analysis. Table 2 shows that both models are within 5% error to the experiment, therefore acceptable.

3.1. Governing equations

Analysed 2D axisymmetric preliminary thermal-FSI model couples solid and fluid domains at the boundaries. In this approach, CSD (computational solid dynamics) analysis is based on the heat conduction equations, which is a standard approach in FVM (Finite Volume Method) software. On the fluid side physics is much more complex, which can be described by the set of equations below

$$\frac{\partial}{\partial t}\begin{Bmatrix}\rho\\ \rho\mathbf{v}\\ \rho e\\ \rho k\\ \rho\varepsilon\end{Bmatrix} + \mathrm{div}\begin{Bmatrix}\rho\mathbf{v}\\ (\rho\mathbf{v}\otimes\mathbf{v}) + p\mathbf{I}\\ (\rho e + p)\mathbf{v}\\ \rho\mathbf{v}k\\ \rho\mathbf{v}\varepsilon\end{Bmatrix} = \mathrm{div}\begin{Bmatrix}0\\ \mathbf{t}^{\mathrm{t}}\\ \mathbf{t}^{\mathrm{t}}\mathbf{v} + \mathbf{q}^{\mathrm{t}}\\ \mathbf{J}_k\\ \mathbf{J}_\varepsilon\end{Bmatrix} + \begin{Bmatrix}0\\ \rho\mathbf{b}\\ \rho S_e\\ \rho S_k\\ \rho S_\varepsilon\end{Bmatrix} \tag{3}$$

where ρ is a density [kg/m^3], **v** represents velocity [m/s], p is a pressure [Pa], **I** is a unit tensor [−], t^{t} is a total viscous stress tensor [Pa], **b** is a gravitation force [N], e represents the sum of specific internal and specific kinetic energy [J/kg], $\mathbf{q}^{\mathrm{t}}$ is a total heat flux [W/m^2], $\mathbf{J}_k$ is a diffusion flux of turbulent kinetic energy k [1/s^3], $\mathbf{J}_\varepsilon$ is a diffusion flux of kinetic energy dissipation ε [1/s^4], S_k represents source of turbulent kinetic energy [m^2/s^3], S_ε is a source of turbulent kinetic energy dissipation [m^2/s^4].

According to Tang et al. study [2], tested case can be well approximated by the k-ε RNG viscus model, which is one of the most popular RANS (Reynolds-Averaged Navier-Stokes) models. However, the full thermal-FSI approach requires analysis of stress, strain and deformation, similar like in article [34].

3.2. Analysed geometries

Sixty-two geometries were analysed in total, which can be group in four categories. First is the reference group, because it contains two geometries experimentally tested by Tang et al. [2] – flat surface and 45 deg. cone. Both models were used to validate analysed FVM model. Second group contains twenty models with cone modification shown on Fig. 2. Radius R_3 was not present in the experiment, but in analysis it varies from 1.4 mm to 20 mm. After results' comparison it can be said that 20 mm arc is so large, that it is an equivalent of a straight line (45 deg. tested cone). Third and fourth groups are similar to the second group, but they contain altered cooling channel height (H = 12 mm and 10 mm) [Fig. 2].

Table 2
Thermal-FSI CFD model validation table.

Cone angle	0 deg.	45 deg.
Experimental $\overline{Nu}$ [−]	1238.7	1343.7
Tang et al. 3D analysis $\overline{Nu}$ [−]	1254.6	1399.1
2D axisymmetric analysis $\overline{Nu}$ [−]	1290.9	1347.2
Tang et al. 3D error [%]	1.3	4.1
2D axisymmetric error [%]	4.2	0.3

3.3. Model summary

The entire 2D axisymmetric thermal-FSI model has been discretized by a quadrilateral dominant mesh, steeply refined in the normal surface direction. Performed sensitivity study proved that further mesh refinement does not change the computational results significantly. Furthermore, consistent mesh refinement was used for all analysed cases, so similar numerical error is expected for all analysed geometries. It has been assumed that the channel's surface is smooth and homogeneous. Wall function Y^+ below one has been implemented for most impingement surface. The standard SIMPLE (semi-implicit method for pressure-linked equations) method was employed for pressure-velocity coupling. The second order upwind schemes were chosen for the solution of the convection term in governing equations. The diffusion terms have been central-differenced with the second order accuracy as well. The detailed methodology of numerical integration regarding the set of governing equations can be found in work [35].

4. Results

4.1. Field of velocity

Velocity plots presented below visualise differences between analysed geometries. Fig. 3 compares two reference cases – flat surface and 45 deg. cone. Water at the room temperature is supplied in the middle and gradually dispersed towards the outlet. First significant difference refers to the stagnation zone located directly below the inlet pipe, where recirculated water reduces impingement effect. In the flat heat sink, recirculation (insulating) bubble is formed due to the fact, that "trapped" fluid is uniformly washed around with no

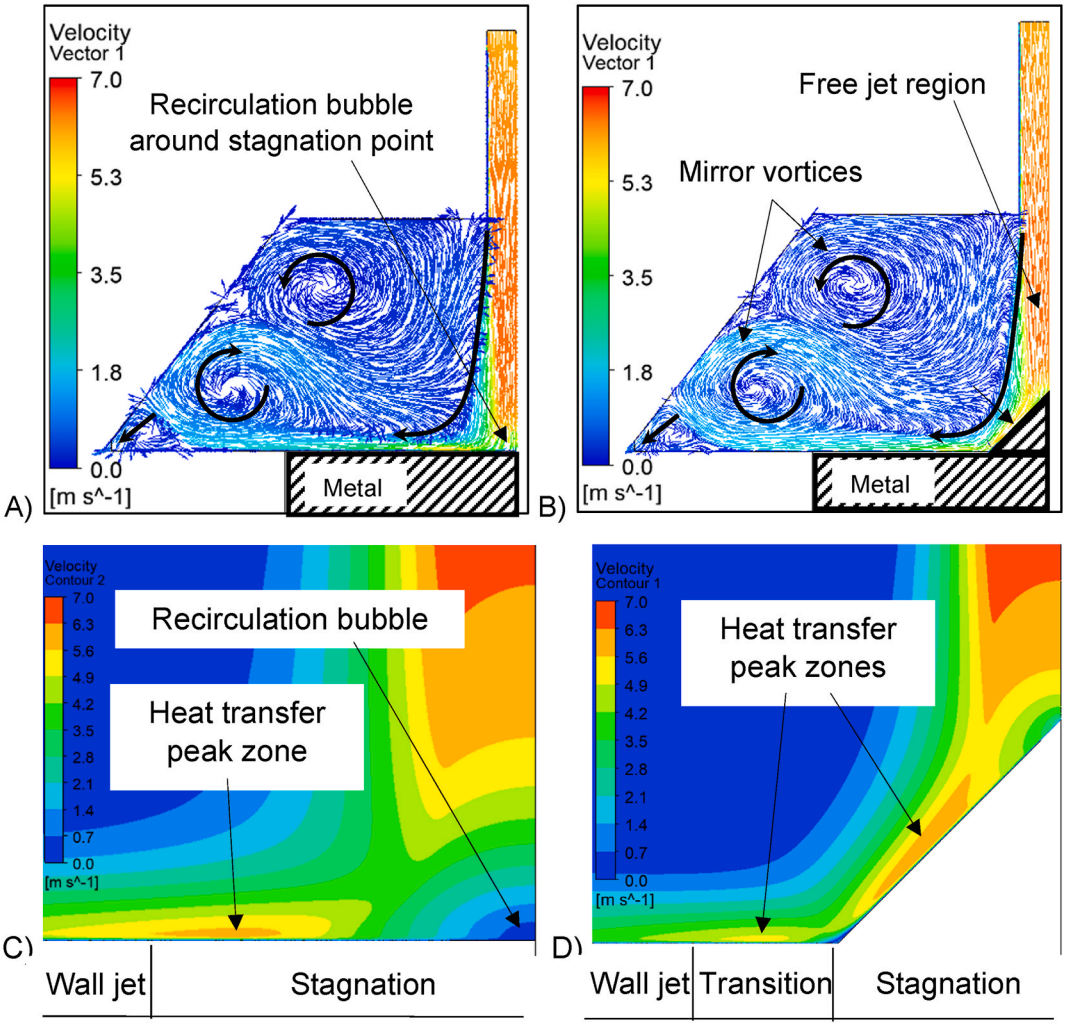

Fig. 3. Reference heat sink velocity ($H = 16$ mm) – A) vector plot of flat case, B) vector plot of 45 deg. cone case, C) contour plot of flat case (detailed view), D) contour plot of smooth cone case (detailed view). *(For interpretation of the references to colour in this figure legend, the reader is referred to the Web version of this article.)*

escape path. That state is improved in the conical heat sink, because described bubble cannot be formed at the tip of the cone. The other key difference is the induction of heat transfer transition zone at the bottom of the cone. High velocity spots along impinged surface mark regions where streamlines have some velocity towards the metal. That creates shear force which reduces the thickness of insulating boundary layer, resulting with heat exchange improvement (heat transfer peak zones on Fig. 3C–D). This is also reflected on Fig. 9, where two Nusselt number peaks are coincident with local high velocity regions.

Fig. 4 presents two extreme geometries from the second group containing nominal height of the cooling channel ($H = 16$ mm). The only difference between them is the radius R_3 (Fig. 2) which affects local Nusselt number distribution. In analysed cases it varies from 1.42 mm to 20 mm, which is very close to the smooth cone ($R_3 = \infty$ mm). That modification introduces additional positive and negative Nusselt number peaks in the middle of the cone (Fig. 9). The second pair of peaks at the cone's bottom are present in the tested smooth cone, but R_3 arc modifies their sizes. Negative peaks are well shown on Fig. 4A as low velocity spots on both sides of R_3 arc. These recirculation zones are caused by the surface discontinuity. Two positive Nusselt number peaks are presented on Fig. 4B as high velocity spots on both sides of cone's bottom. Upper one is affected by R_3 arc, which redirects streamlines resulting in reduction of insulating boundary layer. Lower high velocity spot is driven by the flow's impingement into the flat base surface.

Fig. 5 presents a pair of velocity plots obtained for narrow cooling channel ($H = 10$ mm). Flow structure and description are similar to the nominal case ($H = 16$ mm on Fig. 4), but the main recirculation zone is restricted due to the reduced channel's height. That modification is influential to the average Nusselt Number.

4.2. Cooling efficiency

Fig. 6 presents a summary of all analysed geometries (apart from two reference cases). Each curve for given channel height "H" is based on twenty R_3 analysis points at 1-mm step. The reference "H" height is 16 mm, as it was used in the experiment performed by Tang et al. [2]. Both high performing curves can be divided on four regions – steep initiation below 2 mm, slow climb between 2 and 15 mm, sharp transition between 16 and 17 mm and plateau above 17 mm. Steep initiation region occurs, because the recirculation zone behind the hump decays very quickly with R_3 radius growth. It is caused by the fact, that every hump is consistently fitted at the bottom half of the cone side surface (centre point position is a function of arc size). Slow climb region is formed by the steady heat exchange enhancement at the hump surface and horizontal part below the cone. Following sharp transition region (R_3 between 16 mm and 17 mm) is caused by the interaction between horizontal flow and lower mirror vertex (Fig. 3B). Due to the shape of the fluid domain, part of the horizontal flow is reversed (lower mirror vertex) and such secondary flow interacts with the boundary layer of the horizontal main flow. For low and medium R_3 radiuses (less than 16 mm), this disturbance leads to the consistent Nusselt number improvement at the horizontal surface, which is the most of the heat exchange area. This effect weakens as the cooling passage height decreases. Regarding the plateau zone, Table 3 compares high R_3 cases with the smooth cone ($R_3 = \infty$ mm). It can be concluded that $R_3 > 16$ mm values are very close to the smooth cone, so further R_3 arc increase has a negligible effect to the heat transfer enhancement. The consequence of that is that curves in Fig. 6 are expected to be flat above the value of 16 mm.

Further analysis of Fig. 6 leads to the interesting conclusion that 12 mm channel is generally better than 10 and 16 mm ones (not applicable to the plateau zone). This is another consequence of a complex non-linear hump-driven interaction between primary and secondary flows. A similar type of transition phenomenon was analysed in the work [50], which is based on the dimensionless slip-length (Navier number). It is particularly important in prediction of closures for laminar to turbulent transition undergoing via eddies detachment from the slip layer of nanochannels.

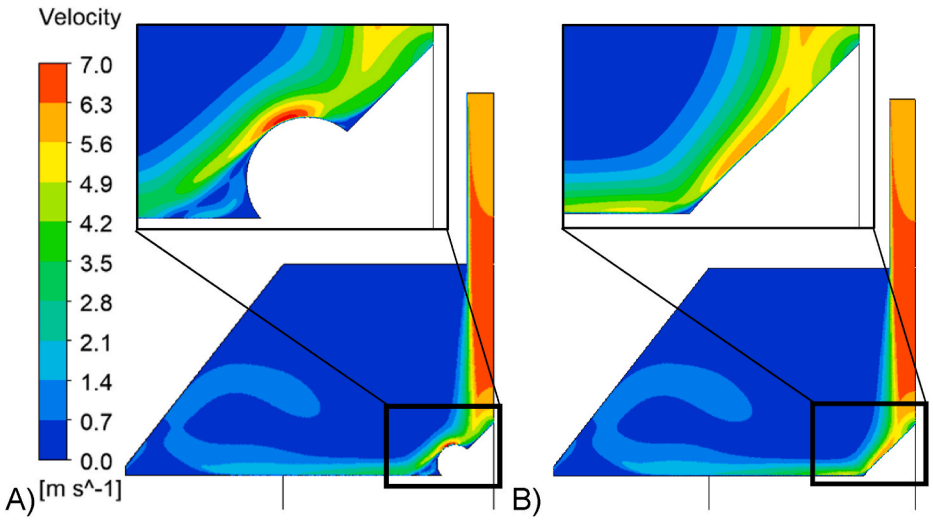

Fig. 4. Heat sink velocity for rounded cone ($H = 16$ mm) – A) $R_3 = 1.4$ mm, B) $R_3 = 20$ mm. *(For interpretation of the references to colour in this figure legend, the reader is referred to the Web version of this article.)*

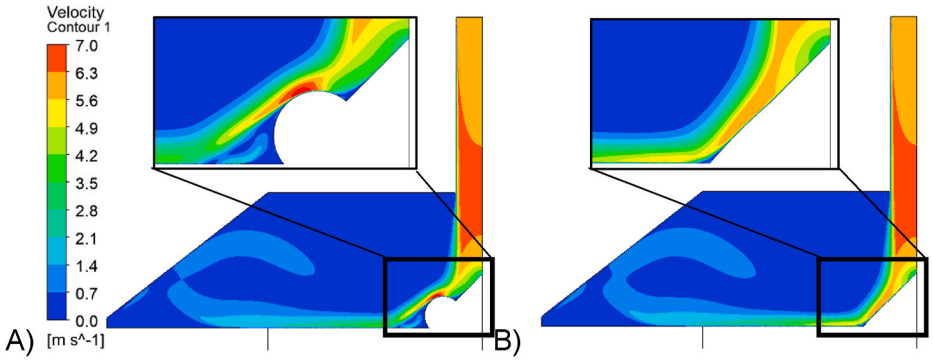

Fig. 5. Heat sink velocity for rounded cone ($H = 10$ mm) – A) $R_3 = 1.4$ mm, B) $R_3 = 20$ mm. *(For interpretation of the references to colour in this figure legend, the reader is referred to the Web version of this article.)*

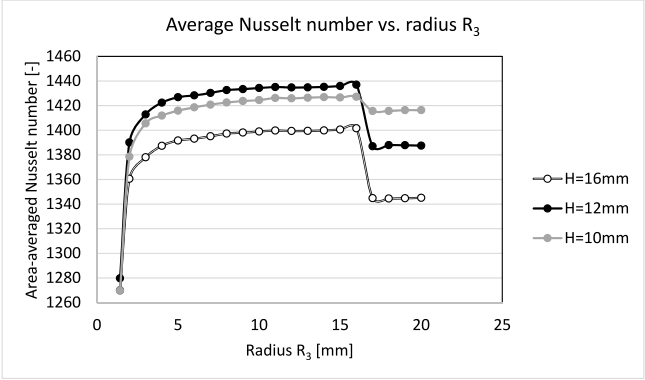

Fig. 6. Area-averaged Nusselt number vs. radius R_3

Table 3
Summary table – Nusselt numbers for high R_3 radiuses.

Average *Nu* [−]	$H = 16$ mm	$H = 12$ mm	$H = 10$ mm
smooth cone	1347.2	1391.3	1417.5
R3 = 20 mm	1345.1	1387.5	1416.3
R3 = 19 mm	1344.7	1387.8	1416.3
R3 = 18 mm	1344.5	1387.9	1415.7
R3 = 17 mm	1344.8	1387	1415.6
R3 = 16 mm	1401.6	1437	1427.2

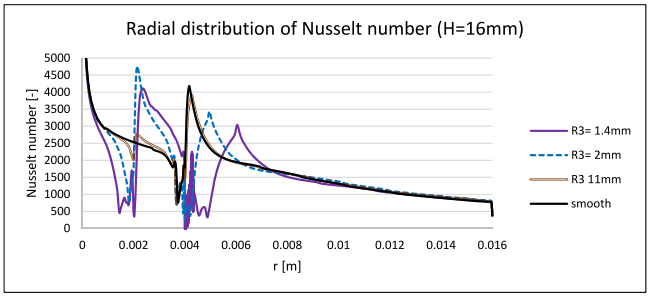

Fig. 7. Radial Nusselt number distribution for chosen R_3 radiuses ($H = 16$ mm).

Comparison between analysed cases revealed, that the best cooling performance occurs at point $H = 12$ mm and $R_3 = 16$ mm. However, that point is at the edge of sharp Nusselt number drop, so tiny R_3 radius variation can cause few percent cooling efficiency drop. From the robustness point of view, the best design point is $H = 12$ mm and $R_3 = 11$ mm.

4.3. Local cooling efficiency

Fig. 7 presents the radial Nusselt number comparison between key R_3 values. The reference curve is the smooth one (cone without R_3 arc), as this is the geometry tested by Tang et al. [2] and used to validate thermal-FSI model.

Fig. 7 presents four of twenty two cases analysed for channel height H = 16 mm. $R_3 = 1.4$ mm is the smallest analysed hump (Fig. 4A), because smaller radius cannot be fitted. Smooth curve is an equivalent of a very large radius ($R_3 = \infty$ mm), so it is an upper limit. Taking this into account, all intermediate radiuses should be placed between those two boundary lines. Due to the geometrical similarities, all four lines have similar regions. Central point (r = 0 mm) is characterised by a very high Nusselt number, because jet is split there at the cone tip. Local minimum around 2 mm radius marks the recirculation point at the hump. Sharp peak afterwards is induced by the local impingement into the hump side surface. Second low point around 4 mm radius is a consequence of recirculation region between the hump and horizontal surface. Sudden peak adjacent to it is driven by the local impingement into the horizontal surface. Its position is a function of the hump radius – the smaller radius, the larger recirculation below it leading to impingement at the higher radius. From Fig. 7 perspective, optimization process should minimise area of low peaks and maximise the impact of positive peaks.

The smallest arc ($R_3 = 1.4$ mm) drops average cooling efficiency even below the flat surface level. The reason being is that small radius creates significant low-performing recirculation regions, which outweigh the improvement at positive Nusselt number peaks. This is reflected is the graph on Fig. 6.

The second analysed arc ($R_3 = 2$ mm) is much better than the smallest one due to the reduction of recirculation zones and shifting them closer to the stagnation point. Fig. 7 shows that positive peaks are also higher, but less influential due to their closer position to the stagnation zone.

Radius $R_3 = 11$ mm is considered as the optimum size from the performance and robustness point of view. In comparison to the smooth-case distribution, it offers advantage due to the second peak region which is not present in the reference (smooth) cone. The other region which is improved in $R_3 = 11$ mm case is the transition zone at the flat heat sink surface ($r > 4$ mm). Fig. 7 shows relatively small impact, but it is significant due to the high radial position.

To properly access the impact of certain zones into the area-averaged Nusselt number, Fig. 7 needs to be normalized into the local heat exchange area. Otherwise it can be incorrectly concluded that the stagnation area has significant impact to the mean heat exchange efficiency. In fact, the stagnation area has a minor effect due to its relatively small area in comparison to the entire heat sink. Fig. 8 presents area-normalized local Nusselt number which is a representation of local contribution into area-averaged Nusselt number. Simple average of Fig. 8 curve is equal to the area-average of Fig. 7 curve. That makes Fig. 8 graph a much clearer representation why one heat sink geometry is better than another. In this case, local Nusselt number comparison is more helpful to make right decision about further shape's improvements.

Detailed analysis of Fig. 8 can help to understand why $R_3 = 11$ mm radius is better than other three cases. It appears that its main advantage over two shorter R_3 radiuses is the smallest recirculation zone at the 4 mm position. Differently from that, advantage over smooth (no hump) curve is distributed mainly along the large horizontal surface. This part of curve is influenced by the complex interaction between main and secondary flows induced by the channel dimensions.

Fig. 8 graph was generated according to the (4). For the visualization process, each curve from Fig. 7 graph was split into 200 equal bands Nu_{ri}, where index i varies from 1 to 200. This equation compares the local stripe's area with the entire heat sink and multiplies it by the local Nusselt number. Constant factor 200 is used for visualization – it converts the under-curve area into the average value on the graph.

The simplification behind the (4) refers to the stagnation area normalization, where all geometries are assumed to be flat. This error can be neglected due to the fact, that affected area is small ($r < 2$ mm), so not very influential to the area-averaged Nusselt number.

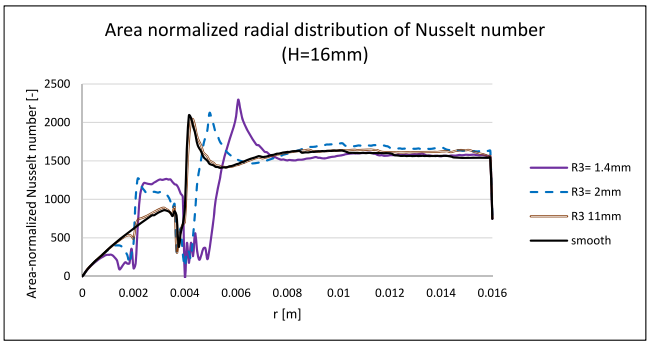

Fig. 8. Area-normalized Nusselt number distribution for chosen R_3 radiuses ($H = 16$ mm).

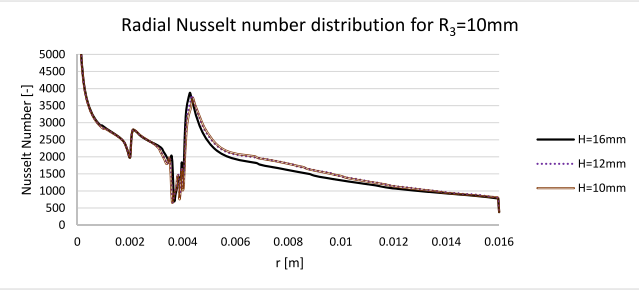

Fig. 9. Radial Nusselt number distribution as a function of channel height *H*.

$$Nu_{rAN\ i} = 200\ Nu_{r\ i}\left(\frac{\pi r_{\ i}^{\ 2} - \pi r_{\ i-1}^{\ 2}}{\pi R_2^{\ 2}}\right) \tag{4}$$

Where: *i* is a radial distance index on Fig. 7 [−], $Nu_{rAN\ i}$ is an area-normalized local Nusselt number on Fig. 8 [−], $Nu_{r\ i}$ is a local Nusselt number on Fig. 7 [−], R_2 is a heat sink radius (Table 1) [m], r_i is a local heat sink radius [m], r_{i-1} is a local heat sink radius preceding to r_i [m].

4.4. Channel height impact

Fig. 9 presents the channel height impact on the Nusselt number radial distribution. It shows clearly why $H = 16$ mm average Nusselt number is worse than 10 mm and 12 mm. The difference is driven by the local Nusselt number difference at the large, horizontal part of the heat sink (r > 5 mm). As mentioned previously, area-averaged Nusselt number is more influenced by the high radiuses due to the area correction. As a consequence of that, modest difference presented in Fig. 9 became significant when comparing area-averaged values.

Heat transfer coefficient at the horizontal part is influenced by the interaction between primary and secondary flow (lower mirror vertex shown on Fig. 3A). Due to the shape of the fluid channel, main flow is split on forward an reversed parts, which eventually are reattached along the horizontal part of heat exchange surface. This reattachment is stronger in the narrower channels, hence the cooling enhancement occurs.

The average change between 10 mm and 12 mm is relatively small, so some secondary effects decide why $H = 12$ mm is better than $H = 10$ mm one.

This paper extends the current knowledge about the single jet impingement system, which most often is based on the flat heat sink. Such cooling system is applicable to the devices, where very dense heat flux is generated over the small area. In such a case, simple extension of heat exchange area is not an option, so cooling enhancement needs to be obtained by the improvement of heat exchange factor. One way to achieve that is the boundary layer thickness reduction by introducing cone in the stagnation area. Such a solution eliminates stagnation recirculating bubble and creates efficient transition zone below the cone (Fig. 3D). That solution is based on the novel single cone heat sink experiment performed by Tang et al. [2].

Presented numerical simulation results explore further improvements of heat sink shape including deformation of the cone side surface. Hump deformation creates a specific step along the washed surface, leading to the induction of local recirculation and secondary impingement zones. Analysis revealed, that for most cases, cooling efficiency balance of those two regions is positive. The only exception is the smallest hump ($R_3 = 1.4$ mm), which has worse performance that the smooth cone.

Presented results should be read from the qualitative and quantitative perspective, as this assessment captures quite a complex interaction between jet, heat sink and fluid channel shape. An important conclusion is that hump has a positive impact to heat exchange intensity, so it can be successfully multiplied forming a series of curved turbulators around the stagnation area. It is recommended to further explore the improvement potential of proposed modifications.

5. Conclusions

This paper extends the current knowledge about the single jet impingement system, which most often is based on the flat heat sink. Such cooling system is applicable to the devices, where very dense heat flux is generated over the small area. In such a case, simple extension of heat exchange area is not an option, so cooling enhancement needs to be obtained by the improvement of heat exchange factor. One way to achieve that is the boundary layer thickness reduction by introducing cone in the stagnation area. Such a solution eliminates stagnation recirculating bubble and creates efficient transition zone below the cone (Fig. 3D). That solution is based on the novel single cone heat sink experiment performed by Tang et al. [2].

Presented numerical simulation results explore further improvements of heat sink shape including deformation of the cone side surface. Hump deformation creates a specific step along the washed surface, leading to the induction of local recirculation and secondary impingement zones. Analysis revealed, that for most cases, cooling efficiency balance of those two regions is positive. The only exception is the smallest hump ($R_3 = 1.4$ mm), which has worse performance that the smooth cone.

Presented results should be read from the qualitative and quantitative perspective, as this assessment captures quite a complex interaction between jet, heat sink and fluid channel shape. An important conclusion is that hump has a positive impact to heat exchange intensity, so it can be successfully multiplied forming a series of curved turbulators around the stagnation area. It is recommended to further explore the improvement potential of proposed modifications.

An area averaged Nusselt number was used as a criterion for the heat enhancement assessment. Main conclusions from this study are listed below:

(1) Cone shape modification can improve heat transfer efficiency of a single cone heat sink. This can be done by introducing a hump in the lower zone of the cone, which resulted in Nusselt number improvement between 1% ($H = 10$ mm channel) and 3% ($H =$ 12 mm channel).
(2) A combined effect of cone modification ($R_3 = 16$ mm) and channel's height reduction ($H = 12$ mm) gives heat transfer enhancement by more than 6.6% in comparison to the reference (smooth) cone. However, for practical application, this improvement is not robust, as it could halve for R_3 arc increase by 1 mm (to 17 mm). That is the reason, why the optimum dimensions are $H = 12$ mm and $R_3 = 11$ mm, which enhance heat transfer by 6.5%.
(3) The comparison between the optimum case ($H = 12$ mm, $R_3 = 11$ mm) and the conventional flat surface heat sink revealed heat transfer enhancement by 11%. This is a combined effect of modified cone and channel's height reduction.
(4) Cone's shape modification based on hump induces two heat transfer transition regions, which can enhance area-averaged Nusselt number. They appear in locations where washed surface is not continuous (hump is not tangent to the adjacent geometry). This is different to the flat surface (no transition region) and to the smooth cone which induces single transition region.

Author statement

Marcin Froissart: conceptualization, formal analysis, data curation, writing - original draft, writing - review and editing. **Paweł Ziółkowski:** investigation, project administration, funding acquisition, **Waldemar Dudda:** methodology, visualization, validation, **Janusz Badur:** resources, supervision.

Declaration of competing interest

The authors declare that they have no known competing financial interests or personal relationships that could have appeared to influence the work reported in this paper.

Acknowledgments

This work was done as a part of PhD thesis at The Institute of Fluid-Flow Machinery of Polish Academy of Sciences. The first author was employed for eight years as a Turbines Mechanical Analyst in Rolls-Royce England, therefore the main motivation behind this work is to explore a potential method of the turbine's cooling system improvement.

The research leading to these presentation has received funding from the Norway Grants 2014–2021 via the National Center for Research and Development.

This paper has been prepared within the frame of the project: "Negative CO2 emission gas power plant" - NOR/POLNORCCS/NEGATIVE-CO2-PP/0009/2019–00 which is co-financed by programme "Applied research" under the Norwegian Financial Mechanisms 2014–2021 POLNOR CCS 2019 - Development of CO2 capture solutions integrated in power and industry processes.

Authors declare no conflict of interest which can bias presented research results.

References

[1] J. Badur, M. Bryk, Accelerated start-up of the steam turbine by means of controlled cooling steam injection, Energy 173 (2019) 1242–1255, https://doi.org/10.1016/j.energy.2019.02.088.
[2] Z. Tang, Q. Liu, H. Li, X. Min, Numerical simulation of heat transfer characteristics of jet impingement with a novel single cone heat sink, Appl. Therm. Eng. 127 (2017) 906–914, https://doi.org/10.1016/j.applthermaleng.2017.08.099.
[3] J. Badur, P. Ziółkowski, W. Zakrzewski, D. Sławiński, S. Kornet, T. Kowalczyk, J. Hernet, R. Piotrowski, J. Felincjancik, P.J. Ziółkowski, An advanced Thermal-FSI approach to flow heating/cooling, J. Phys. Conf. 530 (2014).
[4] F. Afroz, M.A.R. Sharif, Numerical study of heat transfer from an isothermally heated flat surface due to turbulent twin oblique confined slot-jet impingement, Int. J. Therm. Sci. 74 (2013) 1–13.
[5] M. Attalla, H.M. Maghrabie, E. Specht, Effect of inclination angle of a pair of air jets on heat transfer into the flat surface, Exp. Therm. Fluid Sci. 85 (2017) 85–94, https://doi.org/10.1016/j.expthermflusci.2017.02.023.
[6] M. Draksler, B. Koncar, L. Cizelj, B. Niceno, Large Eddy Simulation of multiple impinging jets in hexagonal configuration – flow dynamics and heat transfer characteristics, Int. J. Heat Mass Tran. 109 (2017) 16–27, https://doi.org/10.1016/j.ijheatmasstransfer.2017.01.080.
[7] C. He, Y. Liu, Large-eddy simulation of jet impingement heat transfer using a lobed nozzle, Int. J. Heat Mass Tran. 125 (2018) 828–844.
[8] K. Baghel, A. Sridharan, J.S. Murallidharan, Experimental and numerical study of inclined free surface liquid jet impingement, Int. J. Therm. Sci. 154 (2020), 106389, https://doi.org/10.1016/j.ijthermalsci.2020.106389.
[9] S. Qiu, P. Xu, L. Geng, A.S. Mujumdar, Z. Jiang, J. Yang, Enhanced heat transfer characteristics of conjugated air jet impingement on a finned heat sink, Therm. Sci. 21–1A (2017) 279–288.
[10] Y.T. Yang, H.S. Peng, Numerical study of pin-fin heat sink with un-uniform fin height design, Int. J. Heat Mass Tran. 51 (2008) 4788–4796, https://doi.org/10.1016/j.ijheatmasstransfer.2008.02.017.
[11] A.W. Glaspell, V.J. Rouse, B.K. Friedrich, K. Choo, Heat transfer and hydrodynamics of air assisted free water jet impingement at low nozzle-to-surface distances, Int. J. Heat Mass Tran. 132 (2019) 138–142, https://doi.org/10.1016/j.ijheatmasstransfer.2018.11.173.

[12] P. Xu, A.P. Sasmito, S. Qiu, A.S. Mujumdar, L. Xu, L. Geng, Heat transfer and entropy generation in air jet impingement on a model rough surface, Int. Commun. Heat Mass Tran. 72 (2016) 48–56.
[13] K. Nagesha, K. Srinivasan, T. Sundararajan, Enhancement of jet impingement heat transfer using surface roughness elements at different heat inputs, Exp. Therm. Fluid Sci. 112 (2020), 109995.
[14] P. Singh, M. Zhang, S. Ahmed, K.R. Ramakrishman, S. Ekkad, Effect of micro-roughness shapes on jet impingement heat transfer and fin-effectiveness, Int. J. Heat Mass Tran. 132 (2019) 80–95.
[15] J. Ortega-Casanova, F. Molina-Gonzales, Axisymmetric numerical investigation of the heat transfer enhancement from a heated plate to an impinging turbulent axial jet via small vortex generators, Int. J. Heat Mass Tran. 106 (2017) 183–194.
[16] Y. Rao, P. Chen, C. Wan, Experimental and numerical investigation of impingement heat transfer on the surface with micro W-shaped ribs, Int. J. Heat Mass Tran. 93 (2016) 683–694.
[17] F. Tong, W. Gou, Z. Zhao, W. Gao, H. Li, L. Li, Numerical investigation of impingement heat transfer on smooth and roughened surfaces in a high-pressure turbine inner casing, Int. J. Therm. Sci. 149 (2020), 106186.
[18] P. Singh, S.V. Ekkad, Effects of spent air removal scheme on internal-side heat transfer in an impingement-effusion system at low jet-to-target plate spacing, Int. J. Heat Mass Tran. 108 (2017) 998–1010.
[19] J. Lee, Z. Ren, P. Ligrani, D.H. Lee, M.D. Fox, H.K. Moon, Cross-flow effects on impingement array heat transfer with varying jet-to-target plate distance and hole spacing, Int. J. Heat Mass Tran. 75 (2014) 534–544.
[20] C. Wang, L. Wang, B. Sunden, A novel control of jet impingement heat transfer in cross-flow by a vortex generator pair, Int. J. Heat Mass Tran. 88 (2015) 82–90.
[21] C. Wang, L. Luo, L. Wang, B. Sunden, Effects of vortex generators on the jet impingement heat transfer at different cross-flow Reynolds numbers, Int. J. Heat Mass Tran. 96 (2016) 278–286.
[22] C. Wang, Z. Wang, L. Wang, L. Luo, B. Sunden, Experimental study of fluid flow and heat transfer of jet impingement in cross-flow with a vortex generator pair, Int. J. Heat Mass Tran. 135 (2019) 935–949.
[23] X. Fan, L. Li, J. Zou, Y. Zhou, Cooling methods for gas turbine blade leading edge: comparative study on impingement cooling, vortex cooling and double vortex cooling, Int. Commun. Heat Mass Tran. 100 (2019) 133–145.
[24] A. Azimi, M. Ashjaee, P. Razi, Slot jet impingement cooling of a concave surface in an annulus, Exp. Therm. Fluid Sci. 68 (2015) 300–309.
[25] L. Liu, X. Zhu, H. Liu, Z. Du, Effect of tangential jet impingement on blade leading edge impingement heat transfer, Appl. Therm. Eng. 130 (2018) 1380–1390.
[26] Q. Bian, J. Wang, Y. Chen, Q. Wang, M. Zeng, Numerical investigation of mist/air impingement cooling on ribbed blade leading-edge surface, J. Environ. Manag. 203 (2017) 1062–1071.
[27] T. Guan, J. Zhang, Y. Shan, Effect of offset-jets arrangement on leading edge hot-air heating effectiveness of engine inlet guide strut, Appl. Therm. Eng. 128 (2018) 357–372.
[28] J. Wang, J. Liu, L. Wang, B. Sunden, S. Wang, Conjugated heat transfer investigation with racetrack-shaped jet hole and double swirling chamber in rotating jet impingement, Numer. Heat Tran., Part A: Applications, 73:11 768-787.
[29] J. Zhou, X. Wang, J. Li, Influences of effusion hole diameter on impingement/effusion cooling performance at turbine blade leading edge, Int. J. Heat Mass Tran. 134 (2019) 1101–1118.
[30] K.M. Kim, H. Moon, J.S. Park, H.H. Cho, Optimal design of impinging jets in an impingement/effusion cooling system, Energy 66 (2014) 839–848.
[31] Y. Chen, H. Wei, Y.Q. Zu, Experimental study on the conjugate heat transfer of double-wall turbine blade components with/without pins, Thermal Science and Engineering Progress 8 (2018) 448–456.
[32] G. Nasif, R.M. Barron, R. Balachandar, Simulation of jet impingement heat transfer onto a moving disc, Int. J. Heat Mass Tran. 80 (2015) 539–550, https://doi.org/10.1016/j.ijheatmasstransfer.2014.09.036.
[33] T.M. Jeng, S.C. Tzeng, H.R. Liao, Flow visualizations and heat transfer measurements for a rotating pin-fin heat sink with a circular impinging jet, Int. J. Heat Mass Tran. 52 (2009) 2119–2131.
[34] T. Muszynski, D. Mikielewicz, Structural optimization of microjet array cooling system, Appl. Therm. Eng. 123 (2017) 103–110.
[35] K. Wongcharee, K. Kunnarak, V. Chuwattanakul, A. Eiamsa-ard, Heat transfer rate of swirling impinging jets issuing from a twisted tetra-lobed nozzle, Case Studies in Thermal Engineering 22 (2020), 100780.
[36] L. Xu, T. Yang, Y. Sun, L. Xi, J. Gao, Y. Li, J. Li, Flow and heat transfer characteristics of a swirling impinging jet issuing from a threaded nozzle, Case Studies in Thermal Engineering 25 (2021), 100970.
[37] Y. Amini, M. Mokhtari, M. Haghshenasfard, M.B. Gerdroodbary, Heat transfer of swirling impinging jets ejected from Nozzles with twisted tapes utilizing CFD technique, Case Studies in Thermal Engineering 6 (2015) 104–115.
[38] J. Badur, P. Ziółkowski, D. Sławiński, S. Kornet, An approach for estimation of water wall degradation within pulverized-coal boilers, Energy 92 (2015) 142–152.
[39] M. Banaszkiewicz, On-line monitoring and control of thermal stresses in steam turbine rotors, Appl. Therm. Eng. 94 (2016) 763–776.
[40] T. Ochrymiuk, Numerical investigations of the 3D transonic field and heat transfer at the over-tip casing in a HP-turbine stage, Appl. Therm. Eng. 103 (2016) 411–418.
[41] P. Ziółkowski, J. Badur, P.J. Ziółkowski, An energetic analysis of a gas turbine with regenerative heating using turbine extraction at intermediate pressure - brayton cycle advanced according to Szewalski's idea, Energy 185 (2019) 763–786.
[42] L. Zhang, T. Nazar, M.M. Bhatti, E.E. Michaelides, Stability analysis on the kerosene nanofluid flow with hybrid zinc/aluminum-oxide (ZnO-Al2O3) nanoparticles under Lorentz force, Int. J. Numer. Methods Heat Fluid Flow Vol. (ahead-of-print No. ahead-of-print).
[43] L. Zhang, M.M. Bhatti, E.E. Michaelides, Electro-magnetohydrodynamic flow and heat transfer of a third-grade fluid using a Darcy-Brinkman Forchheimer model, Int. J. Numer. Methods Heat Fluid Flow, 31:8 2623-2639.
[44] R.E. Abo-Elkhair, M.M. Bhatti, KhS. Mekheimer, Magnetic force effects on peristaltic transport of hybrid bio-nanofluid (Au–Cu nanoparticles) with moderate Reynolds number: an expanding horizon, Int. Commun. Heat Mass Tran. 123 (2021), 105228.
[45] M.M. Bhatti, E.E. Michaelides, Study of Arrhenius activation energy on the thermo-bioconvection nanofluid flow over a Riga plate, J. Therm. Anal. Calorim. 143 (2021) 2029–2038.
[46] J. Badur, M. Karcz, M. Lemański, On the mass and momentum transport in the Navier–Stokes slip layer, Microfluidics and Nanofluids 11 (2011) 439.
[47] J. Badur, P.J. Ziółkowski, P. Ziółkowski, On the angular velocity slip in nano-flows, Microfluid. Nanofluidics 19 (2015) 191–198.
[48] P. Ziółkowski, J. Badur, A theoretical, numerical and experimental verification of the Reynolds thermal transpiration law, Int. J. Numer. Methods Heat Fluid Flow 28 (1) (2018) 64–80.
[49] J. Badur, P. Ziółkowski, S. Kornet, T. Kowalczyk, K. Banaś, M. Bryk, P.J. Ziółkowski, M. Stajnke, Enhanced energy conversion as a result of fluid-solid interaction in micro and nanoscale, J. Theor. Appl. Mech. 56 (1) (2018) 329–332.
[50] P. Ziółkowski, J. Badur, Navier number and transition to turbulence, J. Phys. Conf. 530 (2014).